Article

Stress Corrosion Cracking of 316L Stainless Steel Additively Manufactured with Sinter-based Material Extrusion

Ricardo Santamaria , Ke Wang , Mobin Salasi , Mariano Iannuzzi , Michael Y. Mendoza , Md Zakaria Quadir *

Posted Date: 5 May 2023

doi: 10.20944/preprints202305.0272.v1

Keywords: Chloride stress corrosion cracking (CSCC); crack-branching; c-ring specimen; porosity; residual stresses; transgranular cracking

Article

Stress Corrosion Cracking of 316L Stainless Steel Additively Manufactured with Sinter-based Material Extrusion

Ricardo Santamaria [1], Ke Wang [1], Mobin Salasi [1], Mariano Iannuzzi [1], Michael Y. Mendoza [2], and MD Zakaria Quadir [1,3,*]

[1] Curtin Corrosion Centre, Curtin University, Perth, WA, 6102, Australia; ricardo.santamar@postgrad.curtin.edu.au; ke.wang2@curtin.edu.au; mobin.salasi@curtin.edu.au; mariano.iannuzzi@curtin.edu.au
[2] Institute of Naval and Maritime Science, Universidad Austral de Chile, Valdivia, Los Rios, Chile; michael.mendoza@uach.cl
[3] John de Laeter Centre, Curtin University, Perth, WA, 6845, Australia;
* Correspondence: zakaria.quadir@curtin.edu.au

Abstract: This study investigates the stress corrosion cracking (SCC) behavior of type 316L stainless steel (SS316L) produced with sinter-based material extrusion additive manufacturing (AM). This technology has been shown to produce SS316L with microstructures and mechanical properties comparable to its wrought counterpart in the annealed condition. However, despite plenty of research on SCC of SS316L, little is known about SCC in sinter-based AM SS316L. This study focuses on the influence of sintered microstructures on susceptibility to SCC initiation and crack-branching. Custom-made C-rings were exposed to different stress levels in acidic chloride solutions at various temperatures. To better understand the SCC behavior of SS316L, solution-annealed (SA) and cold-drawn (CD) wrought SS316L were tested for comparison. Results showed that sinter-based AM SS316L was more susceptible to SCC initiation than SA wrought SS316L but more resistant than CD wrought SS316L. Moreover, sinter-based AM SS316L showed noticeably better resistance to crack-branching than both wrought SS316L counterparts. The investigation was supported by comprehensive pre- and post-test microanalysis using light optical microscopy (LOM), scanning electron microscopy (SEM), electron backscatter diffraction (EBSD), and micro-computed tomography (micro-CT)

Keywords: chloride stress corrosion cracking (CSCC), crack-branching, c-ring specimen, porosity, residual stresses, transgranular cracking

1. Introduction

Additive manufacturing (AM) concompases the technologies used to create physical objects from digital data by successively joining material [1]. Sinter-based material extrusion, which is one of the AM technologies categorized by the International Organization for Standardization (ISO) [2], is gaining popularity due to its ease of use, low running and maintenance costs, and reduced safety risks [3,4]. This technology has a multi-step approach that incorporates the principles of fused filament fabrication (FFF), also known as fused deposition modelling (FDM), powder metallurgy (PM), and metal injection molding (MIM). The process starts by heating the pre-alloyed powder-bound feedstock to the binder's melting point, and then extruding it through a nozzle to fabricate the so-called "green-part". In the subsequent step, the primary binder is removed through fully immersion in a solvent bath that leaves a component consisting of powder held by the secondary binder. This so-called "brown-part" is still incomplete in terms of engineering properties. Therefore, in the final step, the component is strengthened by heating it just below its alloy melting point, allowing the metal particles to sinter and create a structure that requires minimal post-processing or machining. The resulting sintered microstructure has been reported to have a weak crystallographic texture, relatively large equiaxed grains, and populated with twin boundaries, pores, and oxide inclusions [5-9]. These characteristics diverge from the typical columnar grains found in other AM

 doi:10.20944/preprints202305.0272.v1

technologies where the heat follows the dissipation route, such as laser engineered net shaping (LENS)[10,11], electron beam additive manufacturing (EBAM)[12,13], and laser-based powder bed fusion (LPBF)[14,15].

Stress corrosion cracking (SCC) is a form of damage mechanism that occurs when cracks nucleate from localized corrosion in materials that are susceptible to specific corrosive environments [16-20]. For instance, in stainless steels, cracks start from corrosion pits that create the stress concentration and acidic environment required for cracking [21-27]. The trajectory of the crack is determined by the energy associated with its propagation process. Therefore, secondary cracks, or crack-branching, occur due to the presence of an obstacle or a more energetically favorable path [28]. The presence of a tensile stress, residual or applied, or both, along with a specific corrodent, are required for SCC to occur. Moreover, the cracks can grow and propagate at much lower stress levels than those needed to fracture the material in the absence of the corrodent [16,18,29-32]. Therefore, despite having the appearance of a brittle fracture, SCC can take place in highly ductile materials [16,33,29]. Austenitic stainless steel UNS S31603 (SS316L) is generally considered an excellent material for engineering applications due to its exceptional ductility, weldability, and corrosion resistance [16,34,35]. Its low carbon content (max. 0.035% [36]) has largely eliminated sensitization of its microstructure, which is responsible for intergranular SCC [16,34,35]. However, when exposed to hot environments containing halides, stressed SS316L can still experience transgranular SCC [17,19,32,37]. Consequently, SCC poses a significant threat to the integrity and reliability of equipment in the energy sector, making it crucial to investigate the use of AM to produce SS316L components with enhanced resistance to this damage mechanism.

Among the AM technologies, there has been a significant increase in the use of LPBF to investigate SCC in SS316L due to its ability to produce an alloy with a fully austenitic microstructure [38-40], extremely low porosity [40-42], excellent resistance to localized corrosion [43-45], and outstanding mechanical properties [40-42]. This is due to the distinctive manufacturing process of LPBF, in which a high-intensity laser is programmed to melt layers of powder feedstock that solidify into near-net-shape parts [2,3,46] at cooling rates ranging from 10^3 and 10^7 K/S [47-50]. However, this heating and cooling cycle at each deposited layer results in LPBF-manufactured SS316L with high residual stresses [40,51,52], which are known to increase its susceptibility to SCC [51,53,54].

The objective of this work was to investigate the SCC behavior of SS316L additively manufactured with sinter-based material extrusion, when exposed to different stress levels and temperatures in an acidic chloride environment. The study focused on the impact of its sintered microstructure on the susceptibility to SCC initiation and crack-branching. The outcomes were compared with those obtained from similarly tested wrought SS316L in solution-annealed (SA), and cold-drawn (CD) conditions. The investigation was supported by a comprehensive pre- and post-test microanalysis carried out with techniques such as light optical microscopy (LOM), scanning electron microscopy (SEM), electron backscattered diffraction (EBSD), and micro computed tomography (micro-CT).

2. Materials and Methods

2.1 Materials

The AM SS316L used in this investigation is fabricated using Bound Metal Deposition (BMD) (Desktop Metal, Studio System). The technology includes the following: i) rods of pre-alloyed SS316L powder held in a mix of polymer and wax binder, ii) a FDM 3D printer, iii) a solvent-based debinding unit, iv) a sintering furnace, and v) a cloud-based software to control the process from digital object to sintered part. All BMD SS316L specimens for tensile and SCC testing were produced with the parameters summarized in Table 1. For comparison, commercially available SA wrought SS316L seamless tubes, and CD wrought SS316L rod bars were included in the investigation. The tubes were 22 mm in diameter and 2 mm in thickness, while the rod bars were 25 mm in diameter.

Preprints (www.preprints.org) | NOT PEER-REVIEWED | Posted: 5 May 2023 doi:10.20944/preprints202305.0272.v1

Table 1. Summary of parameters used to manufacture all BMD SS316L test specimens.

Printing parameters		**Debinding parameters**	
Extrude line width:	0.5 mm	Debinding time:	15 h
Deposited layer height:	0.15 mm	Debinding temperature:	50 °C
Contour shell thickness:	1.50 mm	Debinding pressure:	Atmospheric
Extrusion nozzle size:	0.40 mm	**Sintering parameters**	
Extrusion rate:	30 mm/s	Heating rate:	~1.0 °C/min
Extrusion temperature:	175 °C	Thermal debinding temperature:	550 °C
Build plate temperature:	60 °C	Thermal debinding dwell time:	2 h
Sintering scale factors:	X=Y=Z=1.15	Sintering temperature:	1350 °C
Bulk volume raster pattern:	+45°/-45° each layer	Sintering atmosphere:	Ar >99.997% vol.
Infill density:	100%	Sintering dwell time:	2 h
Print orientation:	Vertical (Z)	Cooling rate:	Furnace cooling

2.2 Analytical characterization

Table 2 presents the elemental composition of the BMD SS316L used in this investigation which was externally determined with inductively coupled plasma atomic emission spectroscopy (ICP-AES) analysis. The chemical composition of SA wrought SS316L, and CD wrought SS316L, as given in their material test reports (MTR), are also presented in Table 2. The standard chemical composition of UNS S31603 was added for comparison.

Table 2. Elemental composition in wt% of BMD SS316L, SA wrought SS316L, CD wrought SS316L, and nominal composition of UNS S31603.

Alloy	**Source**	**Fe**	**C**	**Cr**	**Ni**	**Mo**	**Si**	**Mn**	**P**	**S**
BMD SS316L	ICP-AES	Bal.	0.020	16.3	10.4	2.12	0.61	1.22	0.010	0.010
SA SS316L	MTR	Bal.	0.012	16.1	10.1	2.03	0.46	0.92	0.036	0.002
CD SS316L	MTR	Bal	0.019	16.7	10.1	2.03	0.41	1.72	0.024	0.025
UNS S31603	ASTM A213 [36]	Bal.	Max. 0.035	16.0 18.0	10.0 14.0	2.00 3.00	Max. 1.00	Max. 2.00	Max. 0.045	Max. 0.030

Phases were identified via X-ray diffraction (XRD) analysis using a Cobalt K alpha powder diffractometer radiation source operating at 35 kV 40 mA with a LynxEye detector (Bruker, D8 Discover). All XRD data were collected over an angular range of 15° to 135°, a step size of 0.015°, and a time interval of 0.7 s. Content of γ-austenite (FCC), and δ-ferrite (BCC) phases were quantified from XRD spectra as the area of each crystalline peak over the total area of crystalline peaks. Micro-CT analysis was performed on a 2 × 2 × 2 mm^3 cut sample using a 3D X-ray microscope with an exposure energy of 140 kV, during an exposure time of 24 h, and at a pixel resolution of 2.2 µm (Zeiss 520 Versa).

Microstructural characterization was conducted on representative samples that were cut, mounted in cold epoxy resin, manually wet-ground with SiC abrasive papers, and mechanically polished down to 1 µm surface finish. Light optical microscopy (LOM) analysis was conducted on samples chemically etched with a solution containing 100 ml H_2O, 10 ml HNO_3, and 100 ml HCl.

EBSD analysis was conducted on samples that were polished to a mirror surface finish with 0.02 µm colloidal silica, and then ion-milled for 30 min using a beam voltage of 8 kV at a glancing angle of 4° with full cycle rotational movements (TECHNOORG Linda, SEMPrep2). Samples were surface-coated with a carbon film 5 µm thick to prevent electrostatic charging. Microstructures were imaged using secondary electron (SE) and backscatter (BS) detectors coupled to a field emission-scanning electron microscope (FE-SEM) (TESCAN system, CLARA). Elemental composition was mapped with a high-sensitivity Oxford energy-dispersive X-ray spectroscopy (EDS) detection system attached to

Preprints (www.preprints.org) | NOT PEER-REVIEWED | Posted: 5 May 2023 doi:10.20944/preprints202305.0272.v1

the FE-SEM. The content of non-metallic inclusions was quantified from EDS elemental maps by dividing the area of oxides or sulfides over the total area of the map, per ASTM E1245 [55].

EBSD was conducted with an Oxford symmetry EBSD detector in the FE-SEM on 70° tilted samples, at a working distance of 20 mm, with a beam energy of 28 kV, and a beam current of 1 nA. A clean-up process was applied to the data to assimilate any non- or mis-indexed points, ensuring that a maximum of 10% of the points were modified. Grain boundaries were detected with a threshold misorientation of 10° in conjunction with a minimum of 8 pixels of fractional difference of misorientation variation and a kernel size of 3 by 3. Kernel average misorientation (KAM) maps were utilized to investigate the presence of local strain in the microstructures. This analysis was conducted using a 3 by 3 kernel size, a square kernel shape, and a maximum misorientation angle of 5°.

The average grain size was measured as the maximum Feret diameter. Average grain aspect ratio was calculated as the fitted ellipse aspect ratio. Twin content was measured as the fraction length of Σ3 (<111>/60°) boundaries over the total length of γ-austenite (FCC) boundaries. Schmid factor on the γ-austenite (FCC) phase was measured in the plane/direction {111}<110>. All data acquisition and subsequent post-processing were conducted using the software Aztec and AztecCrystal, respectively.

2.3 Mechanical testing

Tensile tests were conducted per ASTM E8 [56]. BMD SS316L and CD wrought SS316L were tested with rectangular specimens, while SA wrought SS316L was tested using tubular specimens with metallic plugs inserted in its ends to ensure a proper grip. All tests were conducted with a 50 kN universal testing machine (UTM, Shimadzu, AGS- X series). Displacements were measured using an axial extensometer with 25 mm of gauge length and +25 mm of travel length (Epsilon TechCorp). The UTM crosshead speed was set to 0.375 mm/min, and the test was stopped once a clear deviation from the initial linear behavior was observed. The actual yield strength (AYS) of each alloy was calculated by intersecting their corresponding stress-strain curves with an 0.2% offset line running parallel to their elastic portion, per ASTM E8 [56]. Figure 1 shows the geometries and dimensions of the tensile specimens.

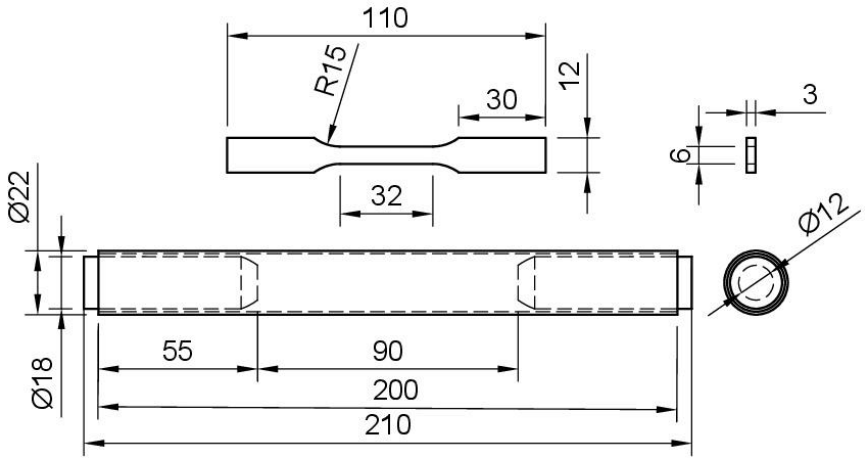

Figure 1. Drawings of the specimens used for tensile testing BMD SS316L and CD wrought SS316L (top), and SA wrought SS316L with snug-fitting metallic plugs (bottom). Units in millimeters.

Microhardness was measured per ASTM E384 [57] using a microhardness tester (Duramin-4, Struers), an applied load of 2 Kg (HV2), and a dwell time of 15 s. The bulk density was determined per ASTM B962 [58], by using a density kit coupled to an analytical balance with a readability of 0.001 g, and a linearity of ± 0.002 g (Mettler-Toledo, ME203). The relative bulk porosity content was calculated as the ratio of the measured bulk density and the standard density of UNS S31603, per ASTM G15 [59].

Preprints (www.preprints.org) | NOT PEER-REVIEWED | Posted: 5 May 2023 doi:10.20944/preprints202305.0272.v1

2.4 SCC susceptibility and crack-branching

The SCC susceptibility of BMD SS316L and its wrought SS316L counterparts was investigated by exposing the alloys to different applied stress and temperature conditions. All tests were conducted using a custom-made C-ring type specimen designed per ASTM G38 [60] and shown in Figure 2. This specimen was selected due to its versatility to be elastically deformed at different magnitudes, unlike the U-bent type suggested by ASTM G123 [61]. Therefore, to further study the impact of multiple stress levels on the susceptibility to SCC, duplicates of BMD SS316 C-rings and their wrought SS316L counterparts were tested under stresses corresponding to 60% and 90% of their AYS. Unstressed C-rings, i.e., 0% AYS, were also tested for comparison. Tests were performed in a 25% (by mass) sodium chloride (NaCl) solution, which was acidified to pH 1.5 with phosphoric acid (H_3PO_4), per ASTM G123 [61]. Nevertheless, since the standard only mentions boiling solution for conducting the tests, the experimental matrix in this investigation was expanded to include solutions at 30 °C, 60 °C, and 80 °C to define operating boundaries of SCC susceptibility under a range of temperatures.

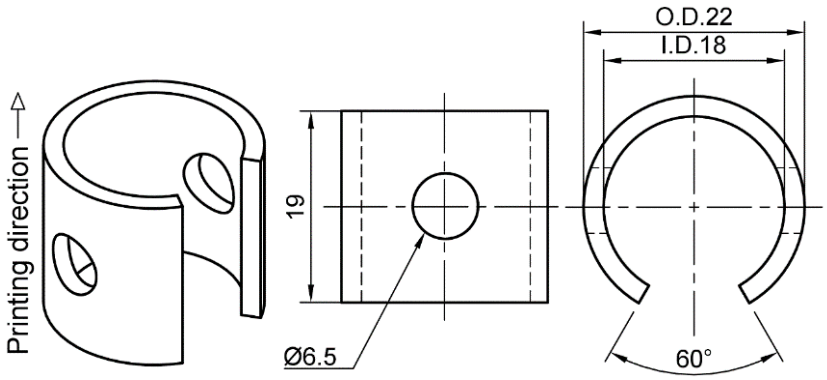

Figure 2. Drawings of the C-ring type specimen used to investigate the SCC susceptibility in the BMD SS316L and its wrought SS316L counterparts. Units in millimeters.

BMD SS316L C-rings were 3D printed in the vertical direction as shown in Figure 2. All their surfaces were carefully wet ground from 80-grit to 600-grit with SiC abrasive paper, avoiding any excessive removal of material. Later, C-rings were constant-strained to the required level, per ASTM G38 [60]. The constant-strain setup, which is shown in Figure 3, consisted of two PEEK washers, two M6 titanium flat washers, one M6 titanium socket cap bolt, one M6 titanium flanged lock nut, and a strip of clear PTFE heat shrinkable tube molded to the bolt. The required strain level was obtained by attaching a 0.3 mm circumferential strain gauge (Tokyo Measuring Instruments, FLAB-03-11-1LJC-F) to the upmost curves surface at the middle of the C-ring's arc and width, as shown in Figure 3. Then, the bolt was tightened until the reading in the data logger (Ahlborn, Almemo 2590) indicated the required strain value corresponding to 60% and 90% AYS. All traces of the strain gauges and adhesive were manually removed with 600-grit SiC abrasive paper. The electrical insulation between the titanium bolt and the C-ring was verified with a digital multimeter. The C-rings tested at 0% AYS were also prepared, as shown in Figure 3, but in this case, no strain was applied. SA wrought SS316L and CD wrought SS316L C-rings were equally prepared for testing.

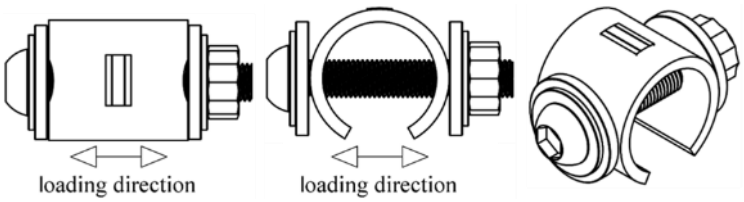

Figure 3. Schematics of the constant-strain setup used to stress the C-rings under different levels of AYS. The circumferential strain gauge is located at the upmost curved surface of the C-ring.

Preprints (www.preprints.org) | NOT PEER-REVIEWED | Posted: 5 May 2023 doi:10.20944/preprints202305.0272.v1

SCC tests were conducted by immersing the C-rings in a series of Erlenmeyer flasks containing 750 ml of solution at constant temperatures. Each temperature was monitored regularly with a thermocouple. Duplicates of stressed and unstressed BMD SS316L C-rings and their wrought counterparts were later immersed in the solution. Each Erlenmeyer flask contained three different C-rings, i.e., one from each alloy stressed at the same level, therefore, the ratio of the volume of solution per exposed surface area of C-ring was 0.112 mm^3/mm^2. All C-rings were placed standing on their washers to ensure that only the test solution was in contact with them. C-rings were removed every week from the solution and inspected for cracks at a magnification of 20X using a LOM. If no cracks were observed, the specimens continued the test in a freshly prepared solution. Inversely, cracked specimens were removed from the test and prepared for microscopy analysis. The tests continued for a maximum of six weeks, per ASTM G123 [61]. In this study, the degree of crack-branching was measured as the total length of cracking, including primary and secondary cracks, divided by the length of the primary crack using LOM images at 10X magnifications. Size and depth of pits were measured per standard ASTM G46 [62].

3. Results

3.1. Analytical characterization

Representative XRD spectra of the BMD SS316 and its wrought counterparts are presented in Figure 4 showing a miscrostructure almost entirely of γ-austenite (FCC) phase with a minor presence of δ-ferrite (BCC) phase. The amount of this secondary phase is summarized in Table 3. The presence of retained δ-ferrite (BCC) in powder-based additively manufactured SS316L can be originated during the gas atomization process of the pre-alloyed powder feedstock due to the ferrite-stabilizer effect of Cr, Mo and Si [41]. Therefore, the slight content found in BMD SS316L suggests that its allotropic transformation into the austenitic matrix was incomplete during the sintering stage.

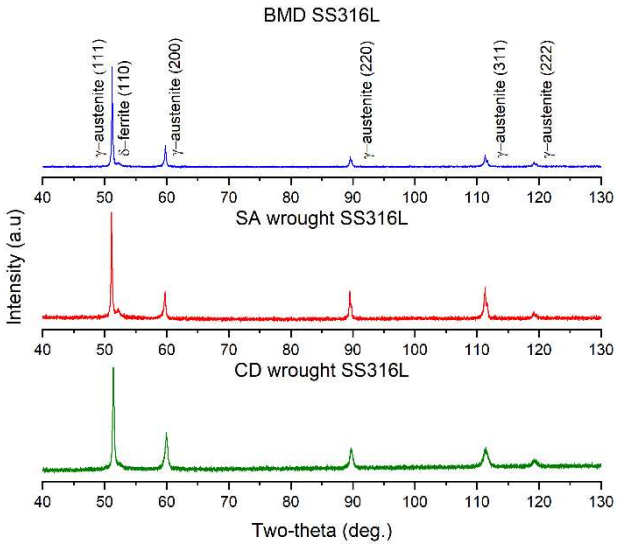

Figure 4. Representative XRD spectra of BMD SS316L, SA wrought SS316L, and CD SS316L showing predominance of the γ-austenitic (FCC) phases with small fractions of δ-ferrite (BCC) phase.

A thorough investigation with EDS analysis showed no evidence of sensitization, i.e., Cr depletion in the vicinity of the grains boundaries, in any of the SS316L alloys as depicted in the elemental map in Figure 5. Nevertheless, BMD SS316L showed non-metallic particles rich in O, Si, Mn, and Cr, as depicted in Figure 5a, which are inherent to PM and MIM manufacturing process [63-65]. SA wrought SS316L showed a slight presence of round pores and no presence of oxide inclusions, as illustrated in Figure 5b. CD wrought SS316L showed the presence of manganese sulfide inclusions (MnS), as depicted in Figure 5c, which are common in cold-worked austenitic stainless steels

Preprints (www.preprints.org) | NOT PEER-REVIEWED | Posted: 5 May 2023 doi:10.20944/preprints202305.0272.v1

[35,66,67]. The content of non-metallic inclusions in BMD SS316L and its wrought counterparts are summarized in Table 3.

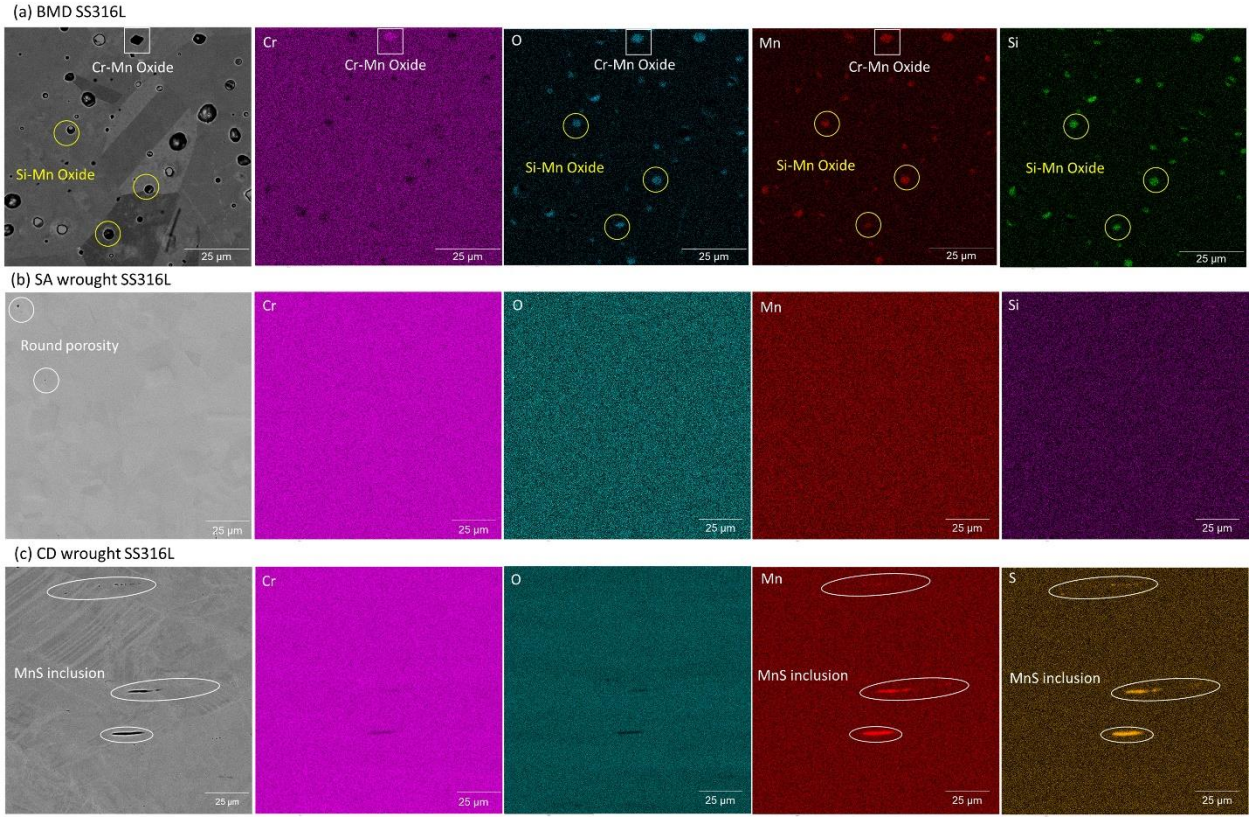

Figure 5. Representative EDS elemental map of a) BMD SS316L showing inclusions rich in O, Si, Mn, and Cr, b) SA wrought SS316L showing slight presence of round pores and lack of non-metallic inclusions, and c) CD wrought SS316L showing elongated MnS inclusions.

Figure 6 shows representative inverse pole figure map EBSD maps with respect to the build direction (Y-axis) of BMD SS316L and its wrought SS316L counterparts. The corresponding {111} pole figures in Figure 6a show a weakly texture, almost randomly oriented distribution with the low intensity (x1.17 random) in the BMD SS316L. In comparison, Figures 6b and 6c show a slight texture strengthening in the wrought SS316L (x2.81 random), and CD wrought SS316 (x2.27 random), respectively. These texture developments are assumed to be caused by their processing history, which is beyond the scope of this study. Figure 6a also shows an elongated pore in the BMD SS316L which is perpendicular to its build direction. This type of porosity is inherent to the extruding nature of FDM manufacturing [68-70].

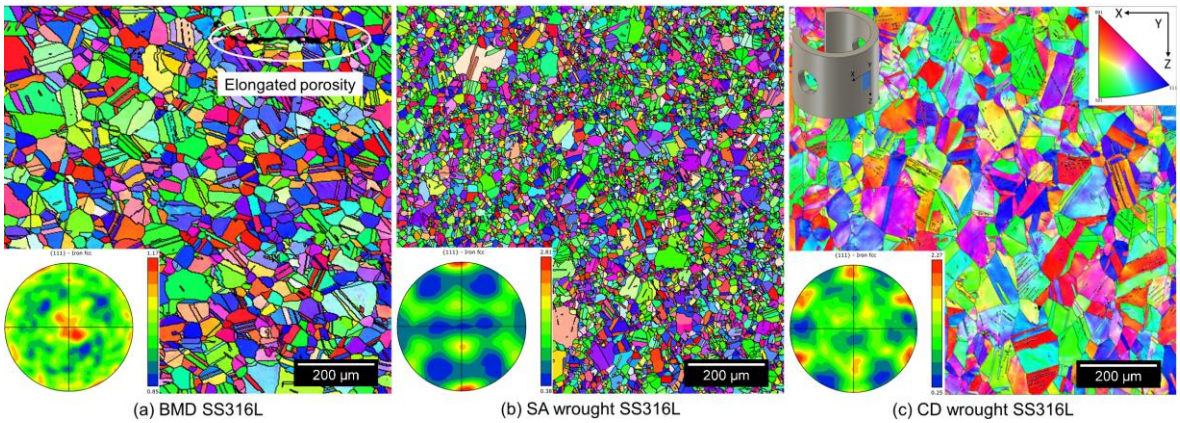

Preprints (www.preprints.org) | NOT PEER-REVIEWED | Posted: 5 May 2023 doi:10.20944/preprints202305.0272.v1

Figure 6. Representative EBSD maps with corresponding inverse pole figures of a) BMD SS316L, b) SA wrought SS316L, and c) CD wrought SS316L C-rings taken from their upmost curved surfaces.

Figure 7, which corresponds to the KAM maps of the scans in Figure 6, shows areas of slight local plastic deformation, i.e., residual stresses, in the microstructure of BMD SS316L. Figure 7b shows a negligible presence of local strain in SA wrought SS316L, as opposed to CD wrought SS316L which can be seen highly populated with residual stresses in Figure 7c. The distinct degree of residual stresses observed in the wrought materials is caused by their processing conditions which are beyond the scope of this study. Grain measurements such as average grain size, aspect ratio, twin boundary content, and Schmid factors of BMD SS316L and its wrought counterparts are included in Table 3.

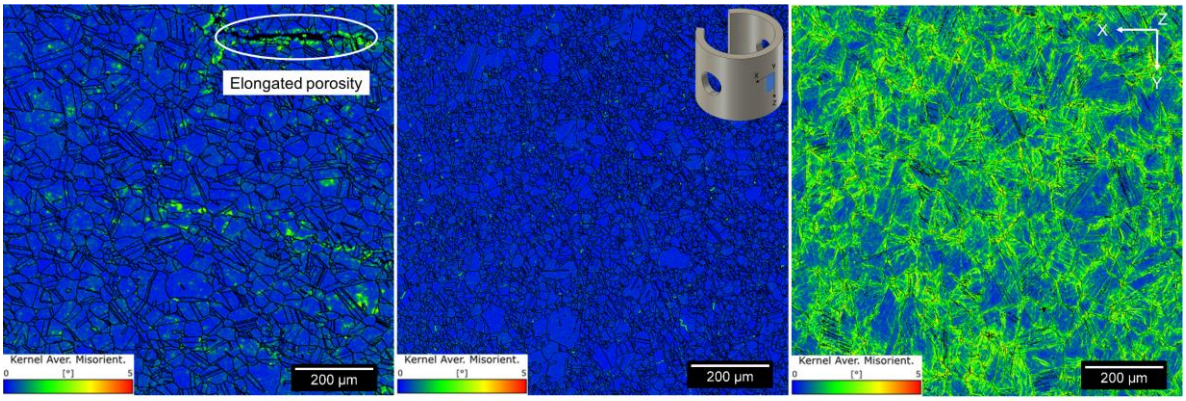

(a) BMD SS316L (b) SA wrought SS316L (c) CD wrought SS316L

Figure 7. Representative KAM maps with a maximum misorientation angle of 5° in a) BMD SS316L, b) SA wrought SS316L, c) CD wrought SS316 C-rings taken from their upmost curved surfaces.

Table 3. Content of non-metallic inclusions, δ-ferrite (BCC) phase, and grain size measurements of BMD SS316L, SA wrought SS316L, and CD wrought SS316L.

Alloy	Non-metallic inclusions (%)	δ-ferrite phase (%)	Average grain size (µm)	Aspect ratio	Twin boundaries (%)	Schmid factor {111}<110>
BMD SS316L	3.23	6.09	40.8 ± 23.8	3.1 ± 2.4	53.2	0.69
SA SS316L	0.01	7.86	16.2 ± 8.5	2.2 ± 1.3	45.5	0.94
CD SS316L	0.39	0.95	43.5 ± 33.6	3.9 ± 3.6	39.4	0.96

3.2 Mechanical testing

Figure 8 presents the elastic regions of the engineering stress-strain curves of BMD SS316L and its wrought SS316L counterparts along with their corresponding 60% and 90% AYS. As depicted in this figure, the CD wrought SS316L, which is in a deformed state, has the highest average value with an AYS of 646 ± 8 MPa, followed by the SA wrought SS316L with 293 ± 6 MPa, and lastly, the BMD SS316L with 167 ± 2 MPa. Similar values of AYS in AM sinter-based SS316L have been reported elsewhere [8,71-73]. Microhardness, bulk density, and relative bulk porosity content of BMD SS316L and its wrought counterparts are presented in Table 4.

Preprints (www.preprints.org) | NOT PEER-REVIEWED | Posted: 5 May 2023 doi:10.20944/preprints202305.0272.v1

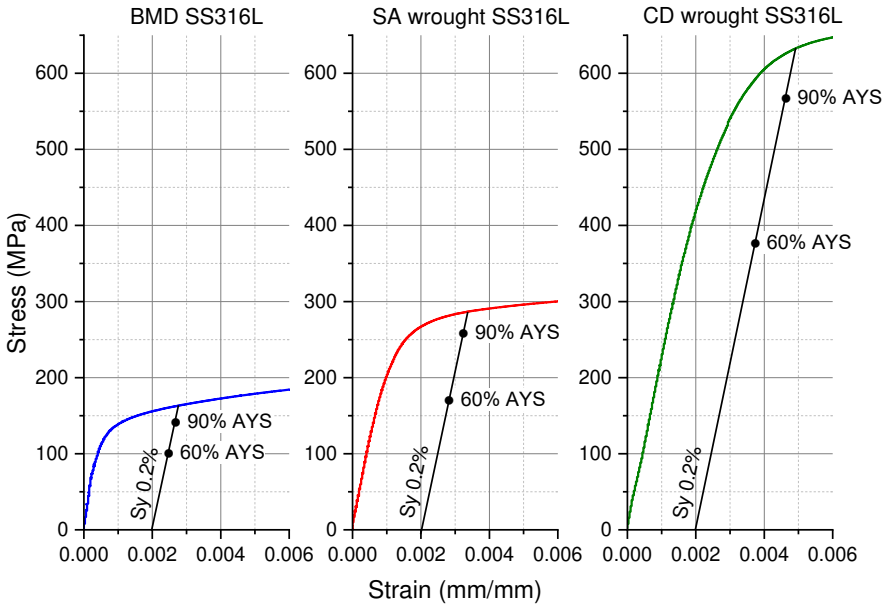

Figure 8. Stress-strain curves within the elastic region of BMD SS316L, SA wrought SS316L, and CD wrought SS316L showing their corresponding 60% and 90% AYS.

Table 4. Average mechanical properties of BMD SS316L and its wrought counterparts.

Alloy	AYS (MPa)	Microhardness (HV2)	Bulk density (g/cm³)	Relative bulk porosity (%)
BMD SS316L	167 ± 2	117.1 ± 3.2	7.564 ± 0.013	5.21
SA SS316L	293 ± 6	163.9 ± 2.5	7.935 ± 0.025	0.57
CD SS316L	646 ± 8	277.3 ± 3.2	7.953 ± 0.027	0.35

3.3 Pitting and cracking susceptibility

Figure 9 illustrates the susceptibility to pitting and cracking initiation in BMD SS316L and its wrought counterparts at different levels of stress and temperature over a period of six weeks. The figure shows cells colored in green representing those conditions where no pitting was observed, cells colored in yellow where pitting was observed, and cells colored in red where the alloy cracked. It can be seen from this figure that at 30°C, none of the C-rings showed evidence of pitting during the time of the test. However, pits were observed in all alloys within the first week when exposed to higher temperatures, i.e., 60°C and above. Moreover, for BMD SS316L and CD wrought SS316L under 90% AYS in boiling solution, the pits quickly transitioned into cracks, as depicted by their red cells in Week 1. Figure 9 shows that cracking resistance in all alloys decreased with increasing time, stress, and temperature, which is in agreement with the literature regarding SCC in stainless steels [18,20,33,74]. The figure also shows that SA wrought SS316L had the least SCC susceptibility as depicted by only 2 out of 12 conditions that led to cracking, followed by BMD SS316L with 4 conditions, and finally, CD wrought SS316L with 7 conditions. It is noteworthy to mention that in stressed CD wrought SS316L specimens, all cracks started from the sharp edges of their curved surface, whereas in unstressed specimens, cracks initiated at their flat surface. This could be caused by the residual stresses induced during the manufacturing process and subsequent machining of the C-rings [74-78].

Preprints (www.preprints.org) | NOT PEER-REVIEWED | Posted: 5 May 2023 doi:10.20944/preprints202305.0272.v1

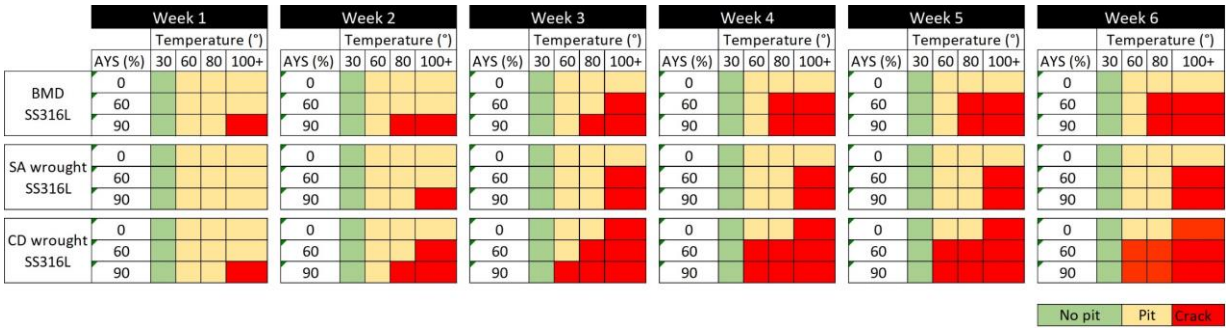

Figure 9. Pitting and cracking susceptibility map of BMD SS316L and its wrought SS316L counterparts at different test conditions over a period of six weeks.

Figure 10 shows the size and distribution of corrosion pits in BMD SS316L unstressed C-rings and wrought counterparts on their flat and curved surfaces after a week of exposure to the boiling solution. The figure shows that the printed material had the biggest pits, while both wrought counterparts showed smaller pits that were similar in size. However, CD wrought SS316L showed a higher amount of pits than the other two alloys. Figure 10 also confirms that unstressed CD wrought SS316L specimens cracked in a week at their flat surface when immersed in boiling solution. Table 5 summarizes the average pit size measurements made on unstressed C-rings after one week in boiling solution, as well as the average pit depth in cracked specimens under stress. The table shows that BMD SS316L had the largest and deepest pits in both measured conditions, while its SA wrought counterpart had the smaller ones.

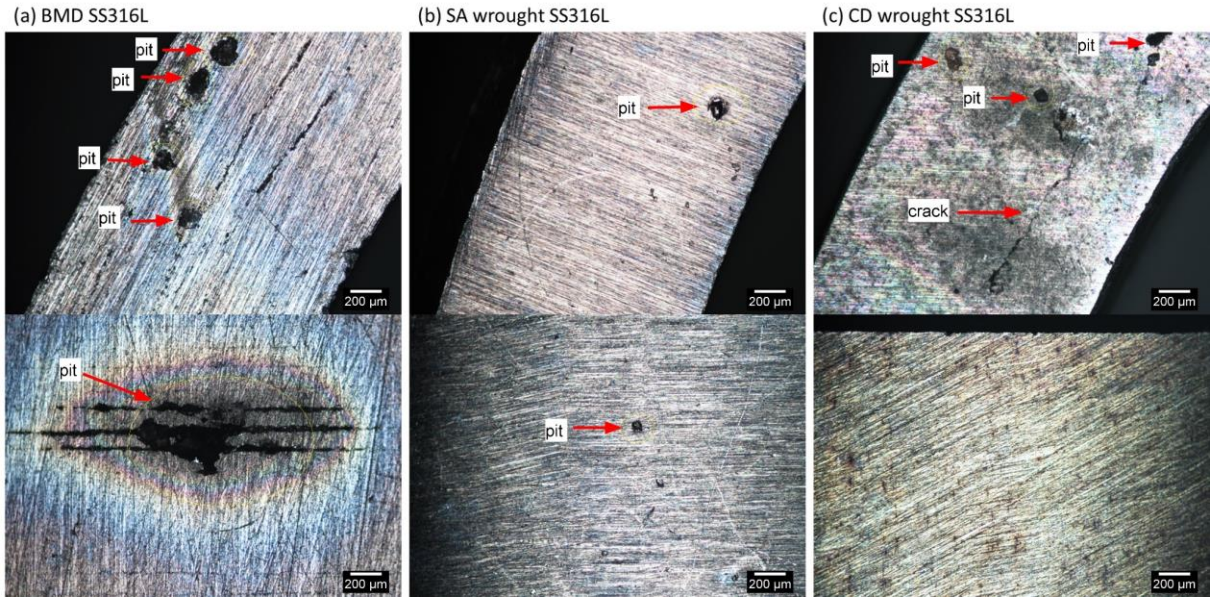

Figure 10. LOM images of unstressed C-rings after one week in boiling solution, showing different sizes of corrosion pits in a) BMD SS316L, b) SA wrought SS316L, and c) CD wrought SS316L. The top images correspond to the C-rings' flat surfaces, while the curve ones are presented at the bottom.

Table 5. Average pit size and pit depth measurements made on stressed and unstressed BMD SS316L C-rings and wrought counterparts.

Alloy	Unstressed C-ring (0%AYS) in boiling solution after 1 week		Stressed C-ring (90%AYS) in boiling solution after cracking	
	Pit size (µm) in flat surface	Pit size (µm) in curved surface	Pit size (µm)	Pit depth (µm)
BMDSS3 16L	112 ± 117	89 ± 154	406 ± 359	190 ± 135

Preprints (www.preprints.org) | NOT PEER-REVIEWED | Posted: 5 May 2023 doi:10.20944/preprints202305.0272.v1

SA SS316L	31 ± 27	28 ± 16	213 ± 178	58 ± 27
CD SS316L	88 ± 61	27 ± 11	205 ± 118	130 ± 84

3.4 Crack-branching susceptibility

Figure 11 shows evidence of transgranular SCC in BMD SS316L and its wrought counterparts after exposure to boiling solution under a stress of 90% AYS. Indentical crack morphology was observed in all specimens regardless of the applied stress and temperature. Evidence of SCC that started from corrosion pits and then propagated perpendicular to the direction of applied stress, which is in agreement with the literature [33,74,79,80], can also be found in Figure 11. This figure also shows that BMD SS316L had the least crack-branching behavior while both wrought SS316L counterparts cracked in a similar fashion. The calculated crack-branching ratio for BMD SS316L, SA wrought SS316L, and CD wrought SS316L was 1.84 μm/μm, 4.29 μm/μm, and 4.64 μm/μm, respectively.

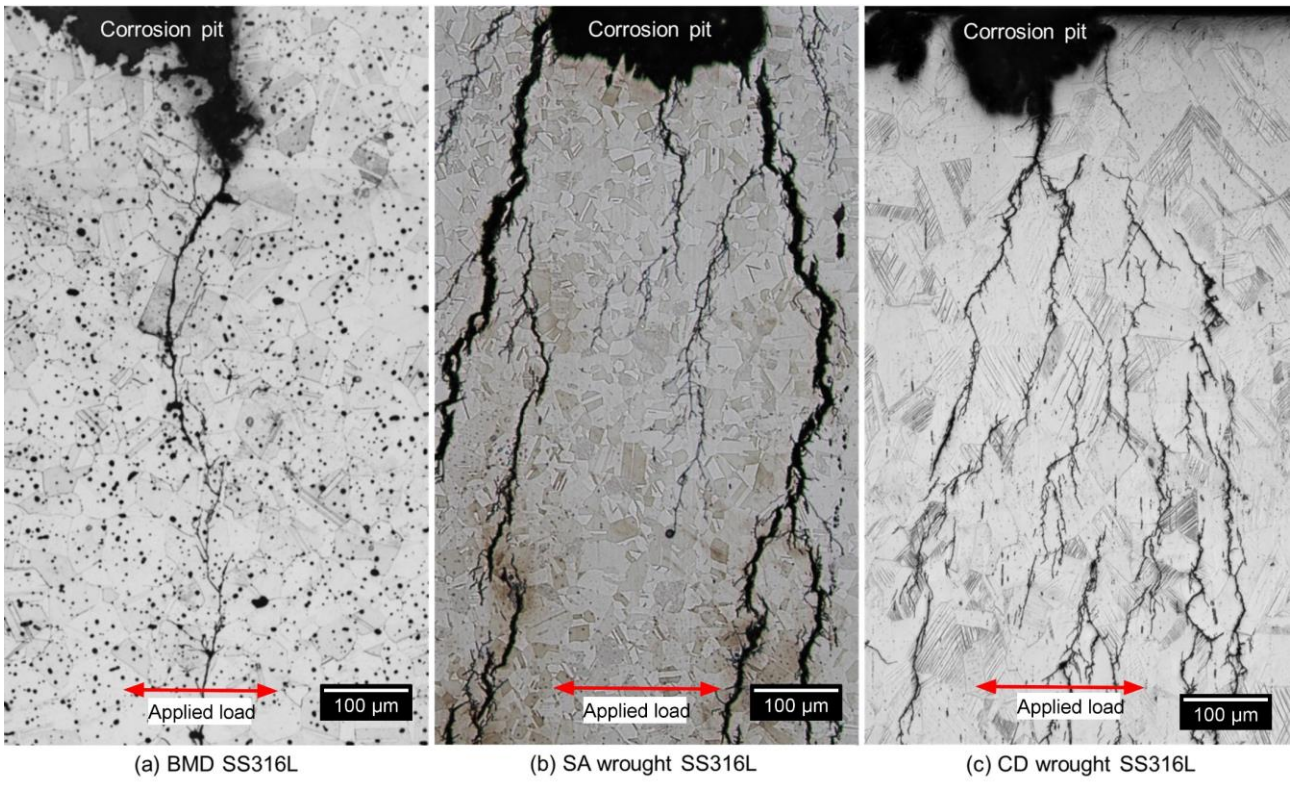

Figure 11. LOM images of etched microstructures in a) BMD SS316L, b) SA wrought SS316L, and c) CD wrought SS316L C-rings after exposure to boiling solution, showing that the SCC initiated from corrosion pits and propagated perpendicular to the applied stress of 90% AYS.

The transgranular nature of SCC in BMD SS316L is also confirmed in the EBSD maps in Figure 12, which displays all Euler map, KAM, and phase distributions along with the overlayed band contrast images to facilitate locating the crack propagations through the grains. It can also be seen form the figure some of the characteristic features of the BMD SS316L microstructure such as twin boundaries, round porosity, oxide inclusions, and δ-ferrite (BCC) as a secondary phase. Additionally, Figure 13 shows a SEM image of a crack that propagated through elongated pores of the printed alloy without any branching. This may be due to the arresting effect of the pores, which is also visible in the micro-CT scan in Supplementary Video 1.

Preprints (www.preprints.org) | NOT PEER-REVIEWED | Posted: 5 May 2023 doi:10.20944/preprints202305.0272.v1

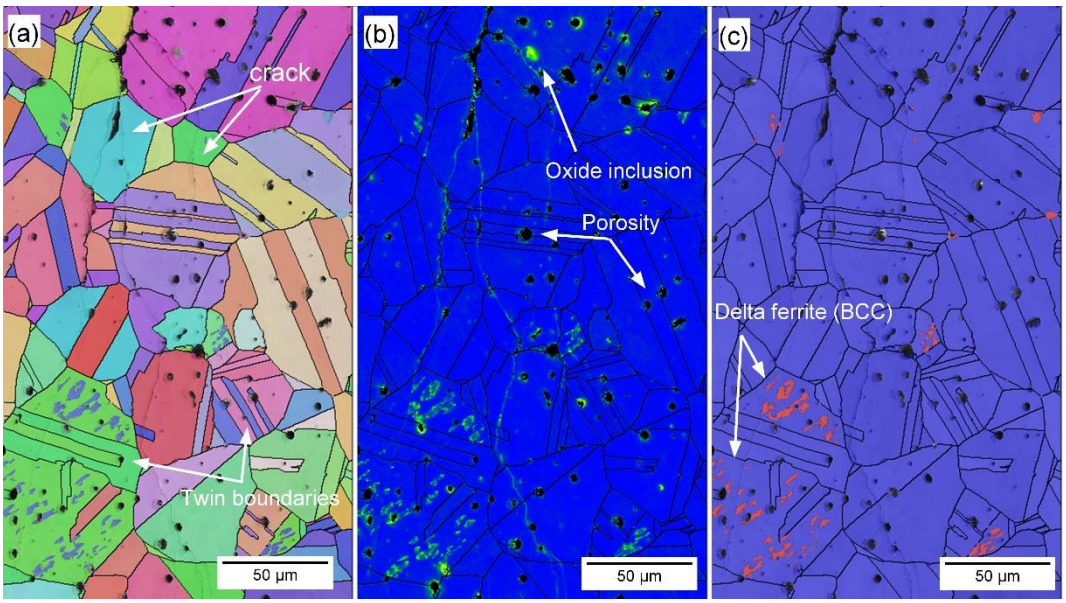

Figure 12. Representative a) EBSD map, b) KAM map, and c) phase map along with the overlayed band contrast of BMD SS316L, showing transgranular cracking, twin boundaries, oxide inclusions, round porosity, and area of δ-ferrite (BCC) phase in its microstructure.

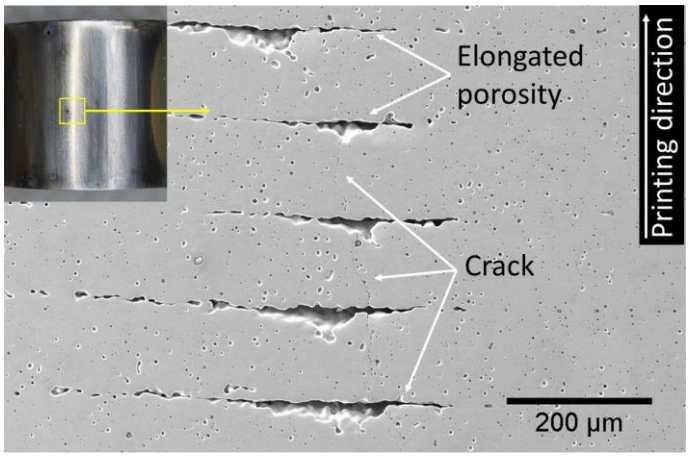

Figure 13. Photographic and SEM image of the curve surface of a BMD SS316L C-ring after exposure to boiling solution under 90% AYS, showing SCC crossing perpendicular to the elongated porosity.

4. Discussion

The results from this study are consistent with the established body of knowledge that non-sensitized austenitic stainless steels under tensile stress are susceptible to transgranular SCC when exposed to hot acidic chloride solutions, i.e., 60 °C or above [16,18,20,34]. Moreover, this study demonstrated that, when tested under the same conditions, BMD SS316L is more susceptible to SCC initiation than SA wrought SS316, but more resistant than CD wrought SS316L, as presented in Figure 9. Nevertheless, highly-branched cracks are a frequent characteristic of SCC [33,37,81], which indicates that BMD SS316L is more resistant to this crack-branching morphology than its wrought counterparts. This is also illustrated in Figure 11. The fact that all alloying compositions in this study were consistent with UNS S31603 [36] suggests that the distinct response of BMD SS316L to SCC initiation and propagation, compared to its wrought counterparts, was influenced by its AM microstructures in terms of defects, as well as, chemistry-phase-crystallography distributions.

Preprints (www.preprints.org) | NOT PEER-REVIEWED | Posted: 5 May 2023 doi:10.20944/preprints202305.0272.v1

4.1 Susceptibility to SCC initiation: pit-to-crack transition

The susceptibility map in Figure 9 shows that CD wrought SS316L has the lowest SCC resistance compared to the other alloys. This can be attributed to its cold-worked condition, which was obtained from a process of plastical deformation that also increased its strength [35,81,82]. This process introduced significant residual stresses, as shown in the KAM map in Figure 7, making it more electrochemically active, and thus, more susceptible to SCC [76]. Additionally, a high-strength steel, such as CD wrought SS316L, as depicted in Figure 8, is expected to have a low stress intensity factor for SCC (K_{iscc}), making it fail under a much lower stress when exposed to a corrosive environment [16,27,31,83]. In comparison, the sintered microstructure of BMD SS316L allowed delay the SCC initiation under more test conditions than its CD wrought counterpart, as presented in Figure 9. This is due to its lack of residual stresses, shown in Figures 7 and 12, and its low-strength behavior, as given in Figure 8. Likewise, the lack of local strain and a relative low strength of SA wrought SS316L were responsible for increasing its SCC resistance.

When BMD SS316L is compared to its SA wrought counterpart, the printed alloy showed a higher susceptibility to SCC. This can be attributed to its higher content of microstructural heterogeneities, such as pores and oxide inclusions, as given in Figure 5, and Tables 3 and 4. These defects create preferred sites for pitting nucleation by weakening the alloy's protective film [65,84-87]. As the pits grow in size, they become more likely to create a more acidic environment and reach the threshold of the alloy's intensity factor, which eventually facilitates the pit-to-crack transition [21-26]. Therefore, the larger and deeper corrosion pits in the microstructure of BMD SS316L, as shown in Figure 10 and reported in Table 5, were the leading cause that decreased its resistance to SCC.

Based on the results showed in this investigation, it can be suggested that the SCC susceptibility of BMD SS316L could be significantly reduced by decreasing the content of porosity and oxide inclusions. This could be achieved by working with low-oxygen powder feedstock or prolonging the sintering time to reduce the size of porosity, albeit grain growth [63-65]. Additionally, post-processing steps such as high isostatic pressure (HIP) could be employed to close the bulk porosity [5,88-91], or shot-peening could be used to close surface pores and introduce compressive residual stresses [92-95].

4.2 Susceptibility to SCC propagation: crack-branching

The noticeable higher resistance to crack-branching observed in BMD SS316L, as illustrated in Figure 11, was attributed to the presence of larger equiaxed grain aggregates that are randomly oriented, with minimal or no influence of special boundaries, and a high content of twin boundaries, which are in general of low energy nature, as presented in Figure 6 and Table 3. These features are commonly found in materials processed with the sinter-based manufacturing technologies [5,8,9,71-73], possessing the microscopy features that serve as barriers for the crack propagation and branching of transgranular SCC. If one focuses on the localized stresses in relation to the lattice, the weakly crystallographic textured microstructure of BMD SS316L led to an overall reduction of the Schmid factor, as given in Table 3, a feature that indicates the requirement of increased resolved shear stress for the initiation of the slip across grains [96-100]. Furthermore, the equiaxed grains are crystallographically randomly oriented and comprise a larger amount of twin boundary fractions in BMD SS316L, thus, enhancing the resistance to crack propagation in nonlocalized directions [97,99-102]. In addition, the higher porosity content in BMD SS316L, also acted as obstacles for crack propagation, leading to weakening the crack progress via branching. A similar arrestor effect, caused by the blunting of the crack tips, has been reported elsewhere in additively manufactured porous alloys [103-105]. The influence of the non-metallic inclusions and retained δ-ferrite (BCC) phase on the resistance to crack-branching could not be determined, since no clear relationship was observed, and hence no further comment can be made, which is subject to the future research.

5. Conclusions

The present study aimed to investigate the SCC behavior of SS316L additively manufactured with sinter-based material extrusion. The study was conducted by exposing stressed and unstressed specimens to acidified chloride solution at different temperatures in comparison to SA wrought SS316L and CD wrought SS316L. This study was monitored via ex-situ microanalysis to understanding cracking behavior in context to the microstructures. Based on the findings, the following conclusions can be made:

1. The sinter-based manufacturing process used to produce BMD SS316L resulted in lower residual stresses and lower strength, which contributed to its higher resistance to the initiation of SCC by making it less electrochemically active.
2. The combination of microscopy features comprising large grain aggregates, equiaxed grain morphology, weak crystallographic texture, and a large content of twin boundaries increases the crack-branching resistance of BMD SS316L.
3. The porosity distribution of BMD SS316L had a mixed impact on its SCC resistance. While these defects accelerated the pit-to-crack transition by weakening the passive film, they also acted as crack arrestors by blunting the crack tips.

Supplementary Materials: The following supporting information can be downloaded at: https://corrosion.box.com/s/b779hpizioe2khsf9mpupdtmoupy5rlv, **Video 1**: Micro-CT scan of BMD SS316L with respect to its build direction (Z) showing the propagation of the secondary cracks being arrested by the elongated porosity.

Author Contributions: Conceptualization, R.S., K.W., M.S., M.I., and Z.Q.; methodology, R.S., M.S., and M.I.; validation, K.W., M.S., and Z.Q.; formal analysis, R.S., K.W., M.S., and M.M.; investigation, R.S.; resources, M.I., and Z.Q.; writing—original draft preparation, R.S.; writing—review and editing, K.W., M.S., M.M., and Z.Q.; supervision, K.W., M.S., and Z.Q.; funding acquisition, M.I., and Z.Q. All authors have read and agreed to the published version of the manuscript.

Funding: This research was funded by the Curtin University of Technology and Woodside Energy, grant number 4610000822.

Institutional Review Board Statement: Not applicable.

Informed Consent Statement: Not applicable.

Data Availability Statement: This article contains all the data that was generated and is presented in the form of Figures, Tables, or Supplementary Materials.

Acknowledgments: The authors acknowledge the financial support of Woodside Energy, as well as the access to the instruments of the Microscopy and Microanalysis Facility (MMF) at the John de Laeter Centre at Curtin University and the Centre for Microscopy, Characterization and Analysis (CMCA) at the University of Western Australia.

Conflicts of Interest: The authors declare no conflict of interest.

References

1. ISO/ASTM-52900 (2015) Additive manufacturing — General principles — Fundamentals and vocabulary. ISO, CH-1211 Geneva 20. doi:https://doi.org/10.1520/F3177-21
2. ISO-17296-2 (2015) Additive Manufacturing - General Principles - Part 2: Overview of process categories and feedstock. ISO International, CH-1211 Geneva 20
3. Redwood B, Schöffer F, Garret B (2017) The 3D printing handbook: technologies, design and applications. 3D Hubs B.V, Amsterdam
4. Poszvek G, Stattler G, Markl E, Seemann R, Lackner M Fused Filament Fabrication of Metallic Components for Semi-professional and Home Use. In: Durakbasa NM, Gençyılmaz MG (eds) Digital Conversion on the Way to Industry 4.0, Cham, 2021// 2021. Springer International Publishing, pp 140-149. doi:https://doi.org/10.1007/978-3-030-62784-3_12
5. Wang Y, Zhang L, Li X, Yan Z (2021) On hot isostatic pressing sintering of fused filament fabricated 316L stainless steel – Evaluation of microstructure, porosity, and tensile properties. Materials Letters 296:129854. doi:https://doi.org/10.1016/j.matlet.2021.129854

6. Thompson Y, Gonzalez-Gutierrez J, Kukla C, Felfer P (2019) Fused filament fabrication, debinding and sintering as a low cost additive manufacturing method of 316L stainless steel. Additive Manufacturing 30:100861. doi:https://doi.org/10.1016/j.addma.2019.100861
7. Jiang D, Ning F (2021) Additive Manufacturing of 316L Stainless Steel by a Printing-Debinding-Sintering Method: Effects of Microstructure on Fatigue Property. Journal of Manufacturing Science and Engineering 143 (9). doi:https://doi.org/10.1115/1.4050190
8. Caminero MÁ, Romero A, Chacón JM, Núñez PJ, García-Plaza E, Rodríguez GP (2021) Additive manufacturing of 316L stainless-steel structures using fused filament fabrication technology: mechanical and geometric properties. Rapid Prototyping Journal 27 (3):583-591. doi:https://doi.org/10.1108/RPJ-06-2020-0120
9. Santamaria R, Salasi M, Bakhtiari S, Leadbeater G, Iannuzzi M, Quadir MZ (2022) Microstructure and mechanical behaviour of 316L stainless steel produced using sinter-based extrusion additive manufacturing. Journal of Materials Science:1-17. doi:https://doi.org/10.1007/s10853-021-06828-8
10. Mendoza MY, Samimi P, Brice DA, Martin BW, Rolchigo MR, LeSar R, Collins PC (2017) Microstructures and grain refinement of additive-manufactured Ti-xW alloys. Metallurgical and Materials Transactions A 48 (7):3594-3605. doi:https://doi.org/10.1007/s11661-017-4117-7
11. Ziętala M, Durejko T, Polański M, Kunce I, Płociński T, Zieliński W, Łazińska M, Stępniowski W, Czujko T, Kurzydłowski KJ, Bojar Z (2016) The microstructure, mechanical properties and corrosion resistance of 316L stainless steel fabricated using laser engineered net shaping. Materials Science and Engineering: A 677:1-10. doi:https://doi.org/10.1016/j.msea.2016.09.028
12. Edwards P, O'Conner A, Ramulu M (2013) Electron Beam Additive Manufacturing of Titanium Components: Properties and Performance. Journal of Manufacturing Science and Engineering 135 (6). doi:https://doi.org/10.1115/1.4025773
13. Wang X, Chou K (2018) EBSD study of beam speed effects on Ti-6Al-4V alloy by powder bed electron beam additive manufacturing. Journal of Alloys and Compounds 748:236-244. doi:https://doi.org/10.1016/j.jallcom.2018.03.173
14. Bahl S, Mishra S, Yazar KU, Kola IR, Chatterjee K, Suwas S (2019) Non-equilibrium microstructure, crystallographic texture and morphological texture synergistically result in unusual mechanical properties of 3D printed 316L stainless steel. Additive Manufacturing 28:65-77. doi:https://doi.org/10.1016/j.addma.2019.04.016
15. Carter LN, Martin C, Withers PJ, Attallah MM (2014) The influence of the laser scan strategy on grain structure and cracking behaviour in SLM powder-bed fabricated nickel superalloy. Journal of Alloys and Compounds 615:338-347. doi:https://doi.org/10.1016/j.jallcom.2014.06.172
16. Jones DA (1996) Principles and Prevention of Corrosion. New international edition. 2nd edn. Pearson, Essex, England
17. Newman RC (2002) Stress-corrosion cracking mechanisms. CORROSION TECHNOLOGY-NEW YORK AND BASEL- 17:399-450
18. McCafferty E (2010) Introduction to corrosion science. Springer Science & Business Media,
19. Zhang W, Fang K, Hu Y, Wang S, Wang X (2016) Effect of machining-induced surface residual stress on initiation of stress corrosion cracking in 316 austenitic stainless steel. Corrosion Science 108:173-184. doi:https://doi.org/10.1016/j.corsci.2016.03.008
20. Spencer D, Edwards M, Wenman M, Tsitsios C, Scatigno G, Chard-Tuckey P (2014) The initiation and propagation of chloride-induced transgranular stress-corrosion cracking (TGSCC) of 304L austenitic stainless steel under atmospheric conditions. Corrosion Science 88:76-88. doi:https://doi.org/10.1016/j.corsci.2014.07.017
21. Bryan CR, Dingreville RPM, Enos D (2016) Estimating Bounding Corrosion Pit Sizes on Stainless Steel SNF Interim Storage Canisters. Sandia National Lab.(SNL-NM), Albuquerque, NM (United States),
22. Martin U, Bastidas DM (2023) Stress corrosion cracking failure analysis of AISI 1018 carbon steel reinforcing bars in carbonated and chloride contaminated environment. Engineering Failure Analysis 147:107159. doi:https://doi.org/10.1016/j.engfailanal.2023.107159
23. Horner DA, Connolly BJ, Zhou S, Crocker L, Turnbull A (2011) Novel images of the evolution of stress corrosion cracks from corrosion pits. Corrosion Science 53 (11):3466-3485. doi:https://doi.org/10.1016/j.corsci.2011.05.050
24. Katona R, Karasz E, Schaller R (2023) A Review of the Governing Factors in Pit-to-Crack Transitions of Metallic Structures. Corrosion 79 (1):72-96
25. Huang X-g, Xu J-q (2013) 3D analysis for pit evolution and pit-to-crack transition during corrosion fatigue. Journal of Zhejiang University SCIENCE A 14 (4):292-299. doi:10.1631/jzus.A1200273
26. Fang BY, Eadie RL, Chen WX, Elboujdaini M (2010) Pit to crack transition in X-52 pipeline steel in near neutral pH environment Part 1 – formation of blunt cracks from pits under cyclic loading. Corrosion Engineering, Science and Technology 45 (4):302-312. doi:10.1179/147842208X386304
27. Marcus P (2011) Corrosion mechanisms in theory and practice. CRC press,

28. Scatigno GG, Ryan MP, Giuliani F, Wenman MR (2016) The effect of prior cold work on the chloride stress corrosion cracking of 304L austenitic stainless steel under atmospheric conditions. Materials Science and Engineering: A 668:20-29. doi:https://doi.org/10.1016/j.msea.2016.05.037
29. Russell HJ (1992) Stress Corrosion Cracking. The Materials Information Society. ASM International, Materials Park, Ohio
30. Sedriks AJ (1996) Corrosion of Stainless Steels. 2nd edn. John Wiley & Sons, Inc, New York
31. Revie RW (2011) Uhlig's Corrosion Handbook. The Electrochemical Society Series, 3rd edn. John Wiley & Sons, Pennington, NJ
32. Raja V, Shoji T (2011) Stress corrosion cracking: theory and practice. Woodhead Publising Limited, Cambridge, UK
33. Jones RH (2017) Stress-Corrosion Cracking: Materials Performance and Evaluation. ASM International. doi:https://doi.org/10.31399/asm.tb.sccmpe2.9781627082662
34. Khatak HS, Raj B (2002) Corrosion of austenitic stainless steels: mechanism, mitigation and monitoring. Woodhead publishing,
35. McGuire MF (2008) Stainless steels for design engineers. Asm International,
36. ASTM-A213 (2022) Standard Specification for Seamless Ferritic and Austenitic Alloy-Steel Boiler, Superheater, and Heat-Exchanger Tubes. ASTM International, West Conshohocken, PA. doi:https://www.astm.org/a0213_a0213m-18.html
37. Newman RC (2011) Stress-corrosion cracking mechanisms. In: Corrosion Mechanisms in Theory and Practice. CRC Press, pp 511-556
38. Liverani E, Toschi S, Ceschini L, Fortunato A (2017) Effect of selective laser melting (SLM) process parameters on microstructure and mechanical properties of 316L austenitic stainless steel. Journal of Materials Processing Technology 249:255-263
39. Woźniak A, Adamiak M, Chladek G, Kasperski J (2020) The Influence of the Process Parameters on the Microstructure and Properties SLM Processed 316L Stainless Steel. Archives of Metallurgy and Materials 65
40. Chao Q, Thomas S, Birbilis N, Cizek P, Hodgson PD, Fabijanic D (2021) The effect of post-processing heat treatment on the microstructure, residual stress and mechanical properties of selective laser melted 316L stainless steel. Materials Science and Engineering: A 821:141611. doi:https://doi.org/10.1016/j.msea.2021.141611
41. Kurzynowski T, Gruber K, Stopyra W, Kuźnicka B, Chlebus E (2018) Correlation between process parameters, microstructure and properties of 316 L stainless steel processed by selective laser melting. Materials Science and Engineering A 718:64-73. doi:https://doi.org/10.1016/j.msea.2018.01.103
42. Suryawanshi J, Prashanth KG, Ramamurty U (2017) Mechanical behavior of selective laser melted 316L stainless steel. Materials Science and Engineering: A 696:113-121. doi:https://doi.org/10.1016/j.msea.2017.04.058
43. Man C, Dong C, Liu T, Kong D, Wang D, Li X (2019) The enhancement of microstructure on the passive and pitting behaviors of selective laser melting 316L SS in simulated body fluid. Applied Surface Science 467-468:193-205. doi:https://doi.org/10.1016/j.apsusc.2018.10.150
44. Shaeri Karimi MH, Yeganeh M, Alavi Zaree SR, Eskandari M (2021) Corrosion behavior of 316L stainless steel manufactured by laser powder bed fusion (L-PBF) in an alkaline solution. Optics & Laser Technology 138:106918. doi:https://doi.org/10.1016/j.optlastec.2021.106918
45. Sander G, Thomas S, Cruz V, Jurg M, Birbilis N, Gao X, Brameld M, Hutchinson CR (2017) On The Corrosion and Metastable Pitting Characteristics of 316L Stainless Steel Produced by Selective Laser Melting. Journal of The Electrochemical Society 164 (6):C250-C257. doi:https://doi.org/10.1149/2.0551706jes
46. Bian L, Shamsaei N, Usher JM (2017) Laser-based additive manufacturing of metal parts: modeling, optimization, and control of mechanical properties. CRC Press,
47. DebRoy T, Wei HL, Zuback JS, Mukherjee T, Elmer JW, Milewski JO, Beese AM, Wilson-Heid A, De A, Zhang W (2018) Additive manufacturing of metallic components – Process, structure and properties. Progress in Materials Science 92:112-224. doi:https://doi.org/10.1016/j.pmatsci.2017.10.001
48. Ma M, Wang Z, Zeng X (2017) A comparison on metallurgical behaviors of 316L stainless steel by selective laser melting and laser cladding deposition. Materials Science and Engineering: A 685:265-273. doi:https://doi.org/10.1016/j.msea.2016.12.112
49. Diaz Vallejo N, Lucas C, Ayers N, Graydon K, Hyer H, Sohn Y (2021) Process Optimization and Microstructure Analysis to Understand Laser Powder Bed Fusion of 316L Stainless Steel. Metals 11 (5):832
50. Tsutsumi Y, Ishimoto T, Oishi T, Manaka T, Chen P, Ashida M, Doi K, Katayama H, Hanawa T, Nakano T (2021) Crystallographic texture- and grain boundary density-independent improvement of corrosion resistance in austenitic 316L stainless steel fabricated via laser powder bed fusion. Additive Manufacturing 45:102066. doi:https://doi.org/10.1016/j.addma.2021.102066

51. Dong P, Vecchiato F, Yang Z, Hooper PA, Wenman MR (2021) The effect of build direction and heat treatment on atmospheric stress corrosion cracking of laser powder bed fusion 316L austenitic stainless steel. Additive Manufacturing 40:101902. doi:https://doi.org/10.1016/j.addma.2021.101902
52. Bian P, Shi J, Liu Y, Xie Y (2020) Influence of laser power and scanning strategy on residual stress distribution in additively manufactured 316L steel. Optics & Laser Technology 132:106477
53. Yazdanpanah A, Franceschi M, Bergamo G, Bonesso M, Dabalà M (2022) On the exceptional stress corrosion cracking susceptibility of selective laser melted 316L stainless steel under the individual effect of surface residual stresses. Engineering Failure Analysis 136:106192. doi:https://doi.org/10.1016/j.engfailanal.2022.106192
54. Yazdanpanah A, Lago M, Gennari C, Dabalà M (2021) Stress corrosion cracking probability of selective laser melted 316l austenitic stainless steel under the effect of grinding induced residual stresses. Metals 11 (2):327
55. ASTM-E1245 (2016) Standard Practice for Determining the Inclusion or Second-Phase Constituent Content of Metals by Automatic Image Analysis. ASTM International, West Conshohocken, PA. doi: https://doi.org/10.1520/E1245-03R16
56. ASTM-E8 (2016) Standard Test Methods for Tension Testing of Metallic Materials. ASTM International, West Conshohocken, PA. doi:https://doi.org/10.1520/E0008_E0008M-16AE01
57. ASTM-E384 (2017) Standard Test Method for Microindentation Hardness of Materials. ASTM International, West Conshohocken, PA. doi:https://doi.org/10.1520/E0384-17
58. ASTM-B962 (2017) Standard Test Methods for Density of Compacted or Sintered Powder Metallurgy (PM) Products Using Archimedes' Principle. ASTM International, West Conshohocken, PA. doi:https://www.astm.org/b0962-17.html
59. ASTM-G15 (2010) Standard Terminology Relating to Corrosion and Corrosion Testing. ASTM International, West Conshohocken, PA 19428-2959 USA
60. ASTM-G38 (2013) Standard practice for making and using C-ring stress-corrosion test specimens. ASTM International, West Conshohocken, PA. doi:https://www.astm.org/g0038-01r21.html
61. ASTM-G123 (2015) Standard test method for evaluationg stress-corrosion cracking of stainless steel alloys with different nickel content in boiling acidified sodium chloride solution. ASTM International, West Conshohocken, PA
62. ASTM-G46 (2018) Standard Guide for Examination and Evaluation of Pitting Corrosion. ASTM International, West Conshohocken, PA 19428-2959 USA
63. German RM (1998) Powder metallurgy of iron and steel. John Wiley & Sons, Inc, 605 Third Ave, New York, NY 10016, USA, 1998. 496.
64. Heaney DF (2012) Handbook of Metal Injection Molding. Woodhead Publishing, Philadelphia, PA
65. Klar E, Samal PK (2007) Powder metallurgy stainless steels: processing, microstructures, and properties. ASM international, Ohio
66. Verhoeven JD (2007) Steel metallurgy for the non-metallurgist. ASM International,
67. Hosford WF (2012) Iron and steel. Cambridge University Press,
68. Yang L, Hsu K, Baughman B, Godfrey D, Medina F, Menon M, Wiener S (2017) Additive manufacturing of metals: the technology, materials, design and production. Springer,
69. Colón Quintana JL, Redmann A, Mazzei Capote GA, Pérez-Irizarry A, Bechara A, Osswald TA, Lakes R (2019) Viscoelastic properties of fused filament fabrication parts. Additive Manufacturing 28:704-710. doi:https://doi.org/10.1016/j.addma.2019.06.003
70. Montero M, Roundy S, Odell D, Ahn S-H, Wright PK (2001) Material characterization of fused deposition modeling (FDM) ABS by designed experiments. Society of Manufacturing Engineers 10 (13552540210441166):1-21
71. Damon J, Dietrich S, Gorantla S, Popp U, Okolo B, Schulze V (2019) Process porosity and mechanical performance of fused filament fabricated 316L stainless steel. Rapid Prototyping Journal 25 (7):1319-1327. doi:https://doi.org/10.1108/RPJ-01-2019-0002
72. Liu B, Wang Y, Lin Z, Zhang T (2020) Creating metal parts by Fused Deposition Modeling and Sintering. Materials Letters 263:127252. doi:https://doi.org/10.1016/j.matlet.2019.127252
73. Gong H, Snelling D, Kardel K, Carrano A (2019) Comparison of Stainless Steel 316L Parts Made by FDM- and SLM-Based Additive Manufacturing Processes. JOM 71 (3):880-885. doi:https://doi.org/10.1007/s11837-018-3207-3
74. Ghosh S, Rana VPS, Kain V, Mittal V, Baveja SK (2011) Role of residual stresses induced by industrial fabrication on stress corrosion cracking susceptibility of austenitic stainless steel. Materials & Design 32 (7):3823-3831. doi:https://doi.org/10.1016/j.matdes.2011.03.012
75. IAEA I (2011) Series, Stress Corrosion Cracking in Light Water Reactors: Good Practices and Lessons Learned, No. NPT-313 IAEA

76. Acharyya SG, Khandelwal A, Kain V, Kumar A, Samajdar I (2012) Surface working of 304L stainless steel: Impact on microstructure, electrochemical behavior and SCC resistance. Materials Characterization 72:68-76. doi:https://doi.org/10.1016/j.matchar.2012.07.008
77. Turnbull A, Mingard K, Lord JD, Roebuck B, Tice DR, Mottershead KJ, Fairweather ND, Bradbury AK (2011) Sensitivity of stress corrosion cracking of stainless steel to surface machining and grinding procedure. Corrosion Science 53 (10):3398-3415. doi:https://doi.org/10.1016/j.corsci.2011.06.020
78. Wenman MR, Trethewey KR, Jarman SE, Chard-Tuckey PR (2008) A finite-element computational model of chloride-induced transgranular stress-corrosion cracking of austenitic stainless steel. Acta Materialia 56 (16):4125-4136. doi:https://doi.org/10.1016/j.actamat.2008.04.068
79. Turnbull A, McCartney LN, Zhou S (2006) A model to predict the evolution of pitting corrosion and the pit-to-crack transition incorporating statistically distributed input parameters. Corrosion Science 48 (8):2084-2105. doi:https://doi.org/10.1016/j.corsci.2005.08.010
80. Turnbull A, McCartney LN, Zhou S (2006) Modelling of the evolution of stress corrosion cracks from corrosion pits. Scripta Materialia 54 (4):575-578. doi:https://doi.org/10.1016/j.scriptamat.2005.10.053
81. Dieter GE, Bacon DJ (1976) Mechanical metallurgy, vol 3. McGraw-hill, New York
82. Callister WD, Rethwisch DG, Blicblau A, Bruggeman K, Cortie M, Long J, Hart J, Marceau R, Ryan M, Parvizi R (2021) Materials science and engineering: an introduction. wiley,
83. Galvele J, Duffó G (1975) Procesos de corrosión. Cursos ECOMAR, Comisión Nacional de Energía Atómica
84. Abbass MK, Ajeel SA, Wadullah HM Biocompatibility, bioactivity and corrosion resistance of stainless steel 316L nanocoated with TiO2 and Al2O3 by atomic layer deposition method. In: Journal of Physics: Conference Series, 2018. vol 1. IOP Publishing, p 012017. doi:https://doi.org/10.1088/1742-6596/1032/1/012017
85. Abdullah Z, Ismail A, Ahmad S The influence of porosity on corrosion attack of Austenitic stainless steel. In: Journal of Physics: Conference Series, 2017. vol 1. IOP Publishing, p 012013. doi:https://doi.org/10.1088/1742-6596/914/1/012013
86. García C, Martín F, de Tiedra P, Cambronero LG (2007) Pitting corrosion behaviour of PM austenitic stainless steels sintered in nitrogen–hydrogen atmosphere. Corrosion Science 49 (4):1718-1736. doi:https://doi.org/10.1016/j.corsci.2006.10.009
87. Deng P, Karadge M, Rebak RB, Gupta VK, Prorok BC, Lou X (2020) The origin and formation of oxygen inclusions in austenitic stainless steels manufactured by laser powder bed fusion. Additive Manufacturing 35:101334. doi:https://doi.org/10.1016/j.addma.2020.101334
88. Mao Y, Yuan J, Heng Y, Feng K, Cai D, Wei Q (2023) Effect of hot isostatic pressing treatment on porosity reduction and mechanical properties enhancement of 316L stainless steel fabricated by binder jetting. Virtual and Physical Prototyping 18 (1):e2174703. doi:https://doi.org/10.1080/17452759.2023.2174703
89. Atkinson H, Davies S (2000) Fundamental aspects of hot isostatic pressing: an overview. Metallurgical and materials transactions A 31:2981-3000. doi:https://doi.org/10.1007/s11661-000-0078-2
90. Teng Q, Xie Y, Sun S, Xue P, Long A, Wu T, Cai C, Guo J, Wei Q (2022) Understanding on processing temperature-metallographic microstructure-tensile property relationships of third-generation nickel-based superalloy WZ-A3 prepared by hot isostatic pressing. Journal of Alloys and Compounds 909:164668. doi:https://doi.org/10.1016/j.jallcom.2022.164668
91. Cai C, Gao X, Teng Q, Kiran R, Liu J, Wei Q, Shi Y (2021) Hot isostatic pressing of a near α-Ti alloy: Temperature optimization, microstructural evolution and mechanical performance evaluation. Materials Science and Engineering: A 802:140426. doi:https://doi.org/10.1016/j.msea.2020.140426
92. Damon J, Dietrich S, Vollert F, Gibmeier J, Schulze V (2018) Process dependent porosity and the influence of shot peening on porosity morphology regarding selective laser melted AlSi10Mg parts. Additive Manufacturing 20:77-89. doi:https://doi.org/10.1016/j.addma.2018.01.001
93. AlMangour B, Yang J-M (2016) Improving the surface quality and mechanical properties by shot-peening of 17-4 stainless steel fabricated by additive manufacturing. Materials & Design 110:914-924. doi:https://doi.org/10.1016/j.matdes.2016.08.037
94. Rautio T, Jaskari M, Gundgire T, Iso-Junno T, Vippola M, Järvenpää A (2022) The Effect of Severe Shot Peening on Fatigue Life of Laser Powder Bed Fusion Manufactured 316L Stainless Steel. Materials 15 (10):3517. doi:https://doi.org/10.3390/ma15103517
95. Jemaa N, Shu J, Kaliaguine S, Grandjean BP (1996) Thin palladium film formation on shot peening modified porous stainless steel substrates. Industrial & engineering chemistry research 35 (3):973-977. doi:https://doi.org/10.1021/ie950437t
96. Lépinoux J, Magnin T (1993) Stress corrosion microcleavage in a ductile f.c.c. alloy. In: Kostorz G, Calderon HA, Martin JL (eds) Fundamental Aspects of Dislocation Interactions. Elsevier, pp 266-269. doi:https://doi.org/10.1016/B978-1-4832-2815-0.50042-5
97. Qu H (2020) Effect of Crystallography On Stress Corrosion Cracking Growth in Austenitic Stainless Steels. Purdue University Graduate School,
98. Hosford W (2009) Mechanical testing. Mechanical behavior of materials:36-64

99. Haidemenopoulos GN (2018) Physical metallurgy: principles and design. CRC Press,
100. Qu HJ, Tao F, Gu N, Montoya T, Taylor JM, Schaller RF, Schindelholz E, Wharry JP (2022) Crystallographic effects on transgranular chloride-induced stress corrosion crack propagation of arc welded austenitic stainless steel. npj Materials Degradation 6 (1):43. doi:https://doi.org/10.1038/s41529-022-00252-2
101. Koyama M, Ogawa T, Yan D, Matsumoto Y, Tasan CC, Takai K, Tsuzaki K (2017) Hydrogen desorption and cracking associated with martensitic transformation in Fe-Cr-Ni-Based austenitic steels with different carbon contents. International Journal of Hydrogen Energy 42 (42):26423-26435. doi:https://doi.org/10.1016/j.ijhydene.2017.08.209
102. Anderson TL (2017) Fracture mechanics: fundamentals and applications. CRC press,
103. Conway KM, Kunka C, White BC, Pataky GJ, Boyce BL (2021) Increasing fracture toughness via architected porosity. Materials & Design 205:109696. doi:https://doi.org/10.1016/j.matdes.2021.109696
104. Kumar P, Jayaraj R, Suryawanshi J, Satwik UR, McKinnell J, Ramamurty U (2020) Fatigue strength of additively manufactured 316L austenitic stainless steel. Acta Materialia 199:225-239. doi:https://doi.org/10.1016/j.actamat.2020.08.033
105. Vieille B, Keller C, Mokhtari M, Briatta H, Breteau T, Nguejio J, Barbe F, Ben Azzouna M, Baustert E (2020) Investigations on the fracture behavior of Inconel 718 superalloys obtained from cast and additive manufacturing processes. Materials Science and Engineering: A 790:139666. doi:https://doi.org/10.1016/j.msea.2020.139666